scientific reports

OPEN

Insights into glucose-derived carbon dot synthesis via Maillard reaction: from reaction mechanism to biomedical applications

Soohyun Cho[1,5], Hyemin Kim[2,5], Dongwook Song[3], Jungchan Jung[3], Sehyeon Park[1], Hyunda Jo[1], Sejeong Seo[1], Chaewon Han[1], Soye Park[1], Woosung Kwon[1,4✉] & Hyunho Han[3✉]

Carbon dots (CDs) are versatile nanomaterials that are considered ideal for application in bioimaging, drug delivery, sensing, and optoelectronics owing to their excellent photoluminescence, biocompatibility, and chemical stability features. Nitrogen doping enhances the fluorescence of CDs, alters their electronic properties, and improves their functional versatility. N-doped CDs can be synthesized via solvothermal treatment of carbon sources with nitrogen-rich precursors; however, systematic investigations of their synthesis mechanisms have been rarely reported. In this study, we developed a method to synthesize N-doped CDs using the Maillard reaction with glucose and ethanolamine as precursors (namely, G-CDs). Comprehensive characterization of these G-CDs revealed the successful incorporation of nitrogen- and glucose-like functionalities. The optical properties and electronic band structures of G-CDs were analyzed using transient absorption and time-resolved photoluminescence spectroscopy. The prepared G-CDs demonstrated near-infrared photoluminescence, low cytotoxicity, glucose transporter-facilitated cellular uptake, and effective heat generation under an 808-nm laser. Particularly, the cellular uptake of G-CDs was reduced by up to 25% after preincubation with a Glut1 inhibitor. These features are suitable for in vitro biological imaging and photothermal therapy in prostate cancer cells. This paper highlights the potential of G-CDs in clinical applications owing to their multicolor emission, photothermal conversion functionality, and versatile surface structure.

Carbon dots (CDs) are carbon-based optical nanomaterials and have garnered significant attention in recent time because of their unique properties and diverse applications in fields such as bioimaging, drug delivery, sensing, and optoelectronics[1–8]. CDs present outstanding photoluminescence (PL) characteristics, exceptional biocompatibility, and remarkable chemical stability[9–14]. Despite the extensive research on CDs, the relatively low quantum yield (QY) is still a significant shortcoming that limits the fluorescence performance and application of CDs[15,16]. Doping CDs with heteroatoms such as nitrogen, sulfur, and other elements significantly enhances their characteristics, resulting in improved fluorescence, altered electronic properties, and increased functional versatility, which boosts the performance of CDs and broadens their applications[17,18].

Nitrogen serves as an efficient dopant because of its atomic size, which closely resembles that of carbon, its strong electronegativity, five valence electrons available for chemical bonding, and a lone electron pair that can be easily transported to the orbitals of sp^2 carbon structures[19–21]. Consequently, numerous studies have investigated the impact of nitrogen doping and other modifications on the electronic structure of CDs[22,23]. Nitrogen doping significantly alters the photophysical characteristics of CDs, including their PL, PL shift, and light absorption[24,25].

[1]Department of Chemical and Biological Engineering, Sookmyung Women's University, 100 Cheongpa-ro 47-gil, Yongsan-gu, Seoul 04310, South Korea. [2]Department of Cosmetics Engineering, Konkuk University, 120 Neungdong-ro, Gwangjin-gu, Seoul 05030, South Korea. [3]Department of Urology, Urological Science Institute, Yonsei University College of Medicine, 50-1 Yonsei-Ro, Seodaemun-gu, Seoul 03722, South Korea. [4]Institute of Advanced Materials and Systems, Sookmyung Women's University, 100 Cheongpa- ro 47-gil, Yongsan-gu, Seoul 04310, South Korea. [5]Soohyun Cho and Hyemin Kim contributed equally to this work. ✉email: wkwon@sookmyung.ac.kr; tintal@yuhs.ac

As N-doped CDs can exhibit a range of N-based chemical structures (e.g., pyridinic, pyrrolic, and graphitic N), N doping can lead to various architectures and occasionally unexpected characteristics[26]. For example, the formation of graphitic or pyrrolic N structures in CDs narrows the CDs' absorption bandgap, which is beneficial for efficient photothermal conversion efficiency (PTE)[27].

N-doped CDs can be synthesized through solvothermal treatment of carbon sources combined with nitrogen-rich molecular precursors. Understanding the mechanism behind nitrogen doping-regulated fluorescent CDs and their applications is therefore highly significant[28]. Recent studies have provided detailed insights into the formation process, molecular structure, and fluorescence mechanisms of N-doped CDs, encouraging further development of N-doped CDs using various precursors[29–32].

Moreover, the reactive groups on the surface of CDs allow for their functionalization with biologically active substances and targeting moieties. At the same time, their inherent fluorescence, combined with minimal cytotoxicity and targeting capability, make them ideal diagnostic agents. These unique attributes position CDs as promising "theranostic" agents, capable of both targeted therapy and diagnosis of diseases, particularly cancer[33–37]. CDs also offer a distinct advantage over other carbon-based nanovectors like carbon nanotubes, or graphene oxides, due to their enhanced safety profile[38–40].

We propose a rational approach for the synthesis of N-doped glucose-derived CDs (G-CDs) based on the Maillard reaction using glucose (GL) and ethanolamine (EA) as precursors. To retain the desirable properties of glucose, we utilized a mild thermal reaction to synthesize N-doped CDs. This approach allowed for the preservation of glucose-like functionalities, thereby imparting additional properties such as biocompatibility and targeting capabilities to the resulting CDs. We have comprehensively characterized the G-CDs, elucidating their nitrogen-containing structures and optical properties. Through transient absorption (TA) and time-resolved PL (TRPL) spectroscopies, we have gained insights into their electronic band structure and charge carrier dynamics. Finally, we demonstrated the cellular uptake of G-CDs can be facilitated by GL transporters and explored the potential of G-CDs for in vitro biological imaging and photothermal therapy (PTT) of lymph node carcinoma of the prostate (LNCaP) cells, leveraging their electron transition and transfer properties. Through this work, we aim to advance the field of CD research by introducing a novel synthesis strategy for N-doped CDs with enhanced properties and potential applications.

Materials and methods
Materials
α-D-GL ($\geq 96\%$), EA ($\geq 98\%$), and deuterium oxide (99.8 at% D, $\geq 99.75\%$) were purchased from Merck. The cellulose ester dialysis tubes were purchased from Spetra/Par Biotech. All the solutions were prepared using triple-distilled water.

Synthesis of G-CDs
To synthesize G-CDs, GL (0.25 g) and EA (2 g) were dissolved in 13 mL of distilled water. The solution was then heated on a hot plate at 200 °C for 12 h for the complete carbonization of GL and EA. A glassy carbon solid formed at the bottom of the reaction vessel, which was subsequently dissolved in water. The crude product yield was approximately 70% or 1.5 g. The resulting CD solution was dialyzed against distilled water for five days using cellulose ester dialysis tubes with a molecular weight cutoff of 100–500 Da. The water was replaced three times daily to ensure the complete removal of residual precursors. After dialysis, the sample was dried through lyophilization, yielding G-CD powders. The final product yield was approximately 45–50% or 1.1–1.2 g.

Material characterizations
Transmission electron microscopy (TEM) analysis was conducted on a JEOL JEM-2200FS instrument equipped with a Cs corrector. The TEM samples were prepared by drop-casting G-CDs dispersed in deionized water onto a carbon-coated copper grid, followed by drying at 80 °C. The particle size distribution and and zeta potential measurements were measured through dynamic light scattering (DLS) with a Horiba SZ-100 particle size analyzer. X-ray diffraction (XRD) patterns were obtained using Cu Kα radiation with a Bruker D8 Advance diffractometer. Raman spectra were acquired using an Alvatek XperRam S spectrometer with 532-nm laser excitation, a 0.5 s acquisition time, and 1.4 mW laser power. X-ray photoelectron spectroscopy (XPS) measurements were performed on a Thermo VG Scientific ESCALAB 250 instrument equipped with a monochromatic Al Kα X-ray source (1486.6 eV) and a magnetic lens. ^{1}H nuclear magnetic resonance (NMR) spectra of GL and G-CDs dissolved in deuterated water (Cambridge Isotope Laboratories) were acquired using a Bruker Avance III HD500 spectrometer (500 MHz). Fourier transform infrared (FTIR) spectra of GL and G-CDs were collected using a Thermo Scientific Nicolet iS50 spectrometer equipped with an attenuated total reflection (ATR) accessory.

Optical characterizations
For all the spectroscopic measurements, the G-CD solutions were sonicated in distilled water to ensure complete and uniform dispersion and 10 mm × 10 mm QS-grade quartz cuvettes (111-QS, Hellma Analytics) were used. Ultraviolet–visible (UV–vis) absorption spectra were recorded using a Scinco S-3100 spectrophotometer. Visible (350–700 nm) PL spectra were acquired using a Jasco FP-8500 fluorometer. Near-infrared (NIR, 700–1200 nm) PL spectra were acquired using a HORIBA PTI QM-500 spectrometer equipped with a 1 W diode laser (660 nm). The absolute QY was determined using a Jasco FP-8500 fluorometer equipped with a 100 mm integrating sphere (ILF-835). The collected data were analyzed using the FWQE-880 Quantum Yield Calculation program. For TA spectroscopy, the G-CDs were diluted in deionized water (0.5 mg/mL) and loaded into a 2 mm thick quartz cuvette. The samples were continuously stirred during the measurements. The TA spectroscopy setup used a regeneratively amplified ytterbium-doped potassium gadolinium tungstate (Yb: KGW) laser (Pharos, Light

conversion) generating photon pulses of 1028 nm wavelength with a pulse duration of 196 fs and a repetition rate of 200 kHz. The fundamental beam was used as the light source, and the pump beam was generated using a harmonic generator (HIRO, Light Conversion) at 258 nm. The pump beam was tuned to a wavelength of 258 nm at a pump power of 4 mW. A portion of the fundamental beam was used as the probe pulse. The probe pulse transmitted through a delay line was focused onto a sapphire plate to generate a white-light continuum using a TA spectrometer (Harpia, Light Conversion) in the visible spectral range of 490–910 nm. The probe beam was subsequently focused onto the sample and overlapped with the pump beam area. The probe beam transmitted through the sample was recorded using a detector (Kymera 193i, Andor). For the TRPL measurements, G-CDs were diluted in deionized water (0.1 mg), loaded into a 2 mm thick quartz cuvette, and continuously stirred. The samples were excited using a regeneratively amplified Yb: KGW laser with a beam radius of 100 μm and a repetition rate of 200 kHz. The excitation pulse was tuned to 400 nm at a power 1 mW of power. Time-correlated single-photon counting (TCSPC) measurements were conducted using a TCSPC module (PicoQuant, PicoHarp 300) attached to a spectrometer (Princeton Instruments, HRS-300) emitting at 480 nm and 1 mW.

Photothermal performance of G-CDs

The G-CDs were dissolved in distilled water at varying concentrations (0, 1, 2, 4, and 10 mg/mL). Each 3 mL G-CD solution was placed in a quartz cuvette and irradiated with 808-nm laser light at 1 W/cm^2 for 10 min. To monitor the photothermal properties of the G-CDs, a thermocouple probe was inserted into the cuvette in direct contact with the G-CD solution, and the temperature was recorded at 1-min intervals.

Cytotoxicity assessment of G-CDs

LNCaP cells were cultured in RPMI-1640 medium supplemented with 1 wt% antibiotic–antimycotic solution and 10 vol% fetal bovine serum (FBS). Then, the cells were seeded at a density of 5×10^3 cells/well in 96-well cell culture plates and incubated for 24 h. The G-CDs were dispersed in RPMI-1640 medium at various concentrations (1, 2, 4, and 10 mg/mL) and added to the wells. The plates were then incubated 37 °C in a humidified 5% CO_2 incubator for 24 h. The resulting cells were washed with PBS and treated with 10% cell counting kit-8 (CCK-8) assay solution in FBS-supplemented media. After a 2-h incubation, the optical density was measured at 450 nm using a SpectraMax M2 microplate reader.

In vitro bioimaging of G-CDs

Fluorescence imaging of LNCaP cells was performed by confocal microscopy. LNCaP cells were prepared in RPMI-1640 medium and seeded (500 μL) in each chamber of a 4-chamber confocal slide for 24 h. The medium was then replaced with 500 μL of RPMI-1640 medium containing 1 mg/mL of G-CDs, followed by incubation at 37°C in a humidified 5% CO_2 incubator for an additional 24 h. Afterward, the cells were washed twice with PBS and fixed using 4% formaldehyde solution. The cells were then stained with a mounting medium containing DAPI (4',6-diamidine-20-phenylindole dihydrochloride). Confocal laser scanning microscopy of the sample-treated cells was performed using a Zeiss LSM 700 confocal microscope with diode-pumped solid-state lasers (488 nm).

Flow cytometry

The cellular uptake of the G-CDs by LNCaP cells was evaluated using flow cytometry. LNCaP cells were maintained under the same conditions as those used in the cell viability test, and cells were seeded on a 12-well plate at a density of 1×10^5 cells per well and incubated for 24 h. To study uptake mechanisms, cells were pre-incubated with a solution of Glut1 inhibitor, STF-31 (1 μM) for 24 h, and incubated with G-CDs for an additional 2 h at 37 °C. The uptake under these inhibitory conditions was compared to the control (inhibitor-free uptake for 2 h at 37 °C). The cells were washed twice with PBS and collected by treating with TrypLE™ Express Enzyme for 3 min. The cells were fixed by 4% (w/v) paraformaldehyde for 15 min, resuspended in PBS, and filtered through a 40 μm mesh to remove aggregates. Each experiment was performed in triplicate. All measurements were performed using a flow cytometer (BD LSRFortessa), and the data were analyzed using FlowJo software.

Photothermal effect of G-CDs in vitro

The photothermal effects of the G-CDs with and without NIR laser irradiation were evaluated in LNCaP cells. Cells were cultured under the same conditions as those used for the cell viability assay and seeded in a 96-well plate. After one day of incubation, G-CDs were added to each well at concentrations of 0, 1, 2, 4, and 10 mg/mL, and the plate was incubated at 37 °C in a humidified 5% CO_2 incubator for 24 h. Following 7-min of exposure to 808-nm laser light at 1 W/cm^2, the cells were incubated for an additional hour. The cells were then washed with fresh PBS and treated with a 10% CCK-8 assay solution in FBS-supplemented medium. After 2 h of incubation, the optical density at 450 nm was measured using a microplate reader. To further evaluate the efficacy of PTT, LNCaP cells (5×10^4 cells in 500 μL per well) were seeded into each chamber of a 4-chamber confocal slide and incubated for 24 h. The cells were then treated with or without G-CDs (4 mg/mL) for 24 h, followed by irradiation with 808-nm laser light (1 W/cm^2) for 7 min. After an additional hour of incubation, the cells were washed with PBS, stained with calcein-AM and propidium iodide, and imaged using an Olympus IX73 inverted microscope.

Statistical analysis

Statistical analysis was performed using the unpaired Student's t-test. Specific pre-processing of the data and sample sizes are described in the figure captions.

Results and discussion
Synthesis and chemical characterization of G-CDs

G-CDs were synthesized by solvothermal carbonization of GL in the presence of EA as a nitrogen source. Figure 1 and Fig. S1 present the proposed mechanism for the formation of N-doped CDs based on the Maillard reaction, which is the reaction between sugars and amino group-containing molecules to produce polymeric or heterocyclic nitrogen compounds. When an aqueous solution of GL was heated at 200 °C with EA, the carbonyl group on GL and amino group on EA condense to produce N-substituted glycosylamine. The glycosylamine compound undergoes Amadori rearrangement to give ketosamine, which then undergoes dehydration and fragmentation to produce N-free compounds such as furfurals, aldehydes, aldols, and N-free polymers. Finally, aldehyde-amine condensation produces heterocyclic nitrogen compounds such as pyridines, pyrazines, and pyrroles, which undergo carbonization to afford CDs with nitrogen-incorporated structures[41–43].

The composition and chemical properties of the G-CDs were characterized using ^{1}H NMR spectroscopy, FTIR spectroscopy, XPS, and elemental analysis. To obtain further insight into the molecular mechanisms driving G-CD formation, G-CDs were synthesized in D_2O, and aliquots of the reaction were collected at various time intervals (ranging from 0 to 12 h without dialysis) for analysis via ^{1}H NMR spectroscopy (Fig. 2a and Fig. S2). The typical peaks of GL located at $\delta = 3$–5 ppm are still observed in the G-CD solution obtained after the thermal reaction and are simplified after dialysis, indicating that the surface structure of GL was partially retained on G-CDs owing to the mild thermal reaction conditions[44,45]. New peaks for alkyl (1.42 ppm), carbonyl (2.02 ppm), alkene (6.59 ppm), and aldehyde (9.37 ppm) were evident in the G-CD solution with a reaction time of 12 h but vanished after dialysis, indicating that small molecules consisting of these kinds of chemical
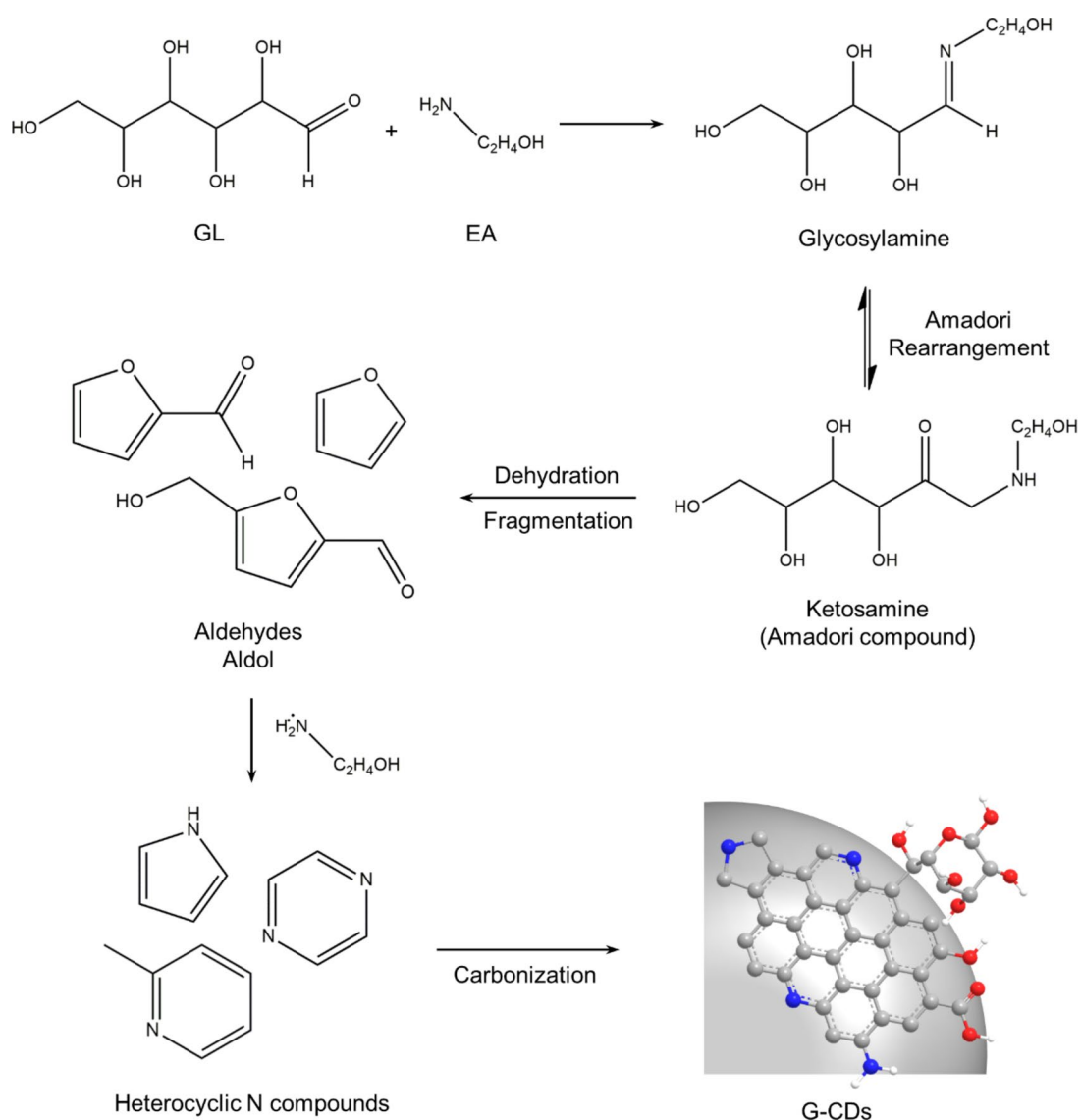

Fig. 1. Proposed mechanism for the formation of G-CDs (gray: carbon, blue: nitrogen, red: oxygen). The gray spheres with an aromatic chemical structure represent the formation of G-CDs with an aromatic core through the carbonization of heterocyclic nitrogen compounds.
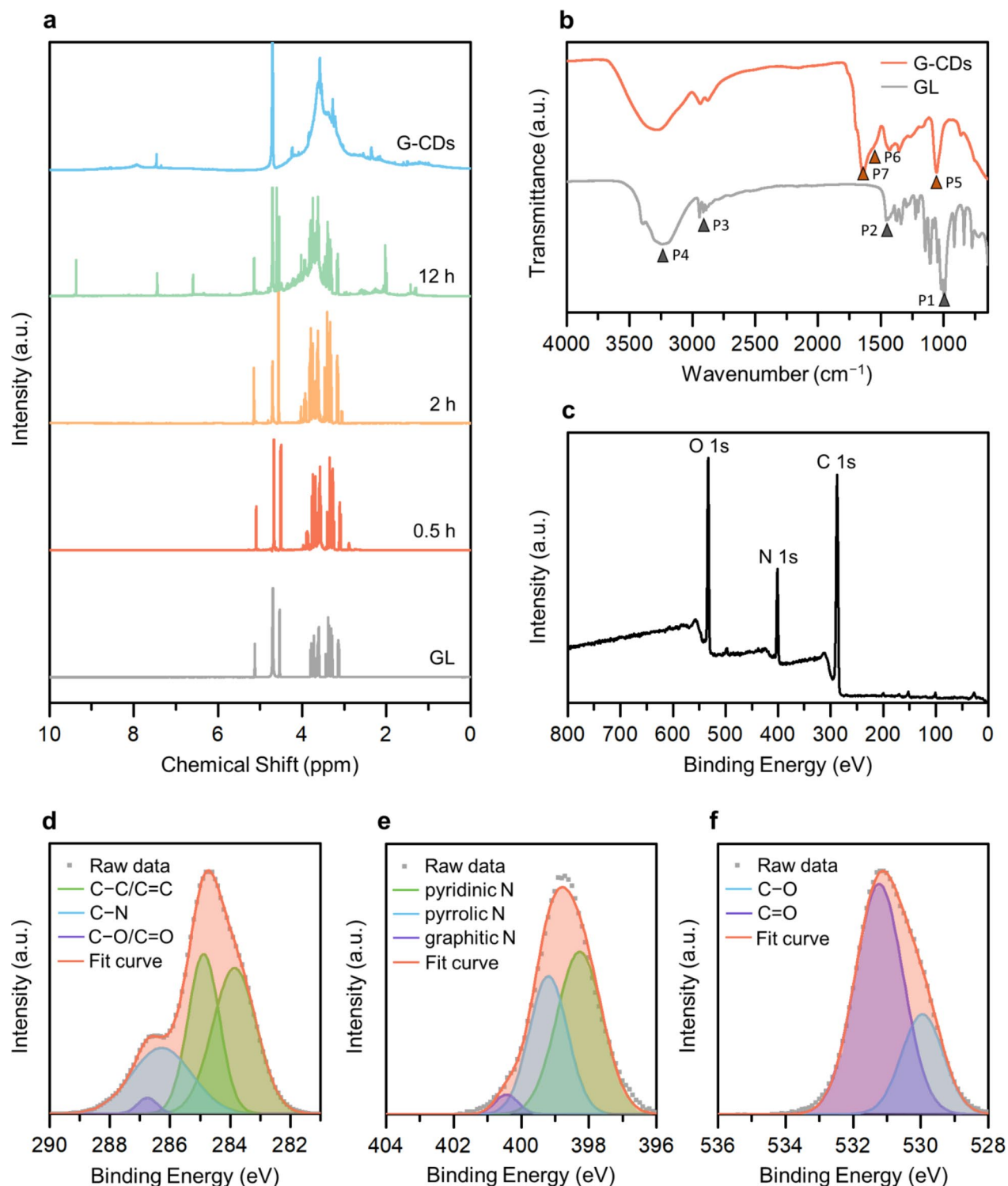
Fig. 2. (**a**) ¹H NMR spectra of GL and G-CDs with different reaction times. The spectra labeled 0.5–12 h correspond to samples collected before dialysis, while the spectrum labeled "G-CDs" represents the sample after dialysis. (**b**) FTIR spectra of GL and G-CDs. (**c**) XPS spectrum of G-CDs. High-resolution (**d**) C 1s, (**e**) N 1s, and (**f**) O 1s XPS profiles of G-CDs.

bonds were generated during the CD reaction process and were removed after dialysis. Typical peaks of the CD structure (2.35, 3.24, 4.23, 7.46, and 7.94 ppm) were evident for the G-CDs. The peaks at 2.35, 4.23, and 7.46 ppm correspond to protons adjoining benzylic, phenol, and aromatic sp² carbons, respectively. After 30 min of reaction, an amine peak appeared at 2.89 ppm, which shifted to 3.06 ppm after 2 h and almost disappeared after 12 h. However, at the same time, the peaks at 3.24 and 7.94 ppm, corresponding to the protons bound to the

aromatic amine and amide groups, respectively, have appeared on G-CDs, indicating the instant release of amine groups and following condensation of nitrogen, which finally ends up with the formation of N-doped CDs. The surface functional groups on the G-CDs were further analyzed using FTIR spectroscopy (Fig. 2b). A typical FTIR spectrum of GL exhibits peaks for C–O stretching (1021 cm^{-1}, P1), C=O stretching (1454 cm^{-1}, P2), C–H stretching (2870–2956 cm^{-1}, P3), and O–H stretching (3075–3420 cm^{-1}, P4), which were also observed in the FTIR spectrum of the G-CDs. This observation is consistent with the ^{1}H NMR analysis (Fig. 2a), indicating that the G-CDs have surface functionalities similar to those of GL[46–48]. In the FTIR spectrum of the G-CDs, aromatic C–N stretching (1178 cm^{-1}, P5), aromatic cyclic C=C stretching (1644 cm^{-1}, P6), and amine N–H bending (1690 cm^{-1}, P7) were observed, indicating the formation of carbon cores with polyaromatic domains and the incorporation of nitrogen into the G-CDs.

Moreover, to determine the electrical charges on the surfaces of the G-CDs, zeta potential analysis was conducted. The zeta potential value of G-CDs was determined to be −30.9 eV (Fig. S3). The negative zeta potential values are due to the presence of electronegative functional groups formed on the surface, especially oxygen-containing functional groups. In addition, several studies have reported that the presence of glucose on the surfaces of particles can lower their electrical charges[49]. The highly negative zeta potential of the G-CDs might be attributed to the cumulative effect of the remaining GL structure on the surface of the G-CDs and the formation of oxygen-containing functional groups originating from the GL and EA precursors on the surface of the G-CDs.

XPS measurements of the G-CDs were conducted to evaluate their chemical structures. The raw XPS data show peaks corresponding to carbon, nitrogen, and oxygen (Fig. 2c). The elemental analysis results in Table 1 show that the carbon content of the G-CDs increased, whereas the oxygen content decreased compared to that of the precursors, which commonly occurs during the carbonization process[50]. Additionally, the G-CDs demonstrated a nitrogen content of 15.1%, indicating that they contained a significant amount of nitrogen atoms that primarily originated from EA.

The carbon 1s spectra depicted in Fig. 2d have peaks at 284.8, 286.3, and 286.8 eV, which correspond to the C–C/C=C, C–N, and C–O/C=O groups, respectively[51]. As shown in Fig. 2e, the nitrogen 1s spectra reveal three distinct peaks at 398.3, 399.2, and 400.4 eV, respectively[52]. These peaks are associated with pyridinic, pyrrolic, and graphitic nitrogen species, indicating the formation of N-doped CDs. In Fig. 2f, the oxygen 1s spectra showed C–O (529.9 eV) and C=O (531.2 eV) peaks, which can be attributed to oxygen-containing defects in the CDs originating from the hydroxyl and carbonyl groups of GL and EA, respectively[53].

Morphological characterization of G-CDs

The morphology and size of the G-CDs were characterized using TEM and DLS. The TEM images revealed well-dispersed G-CDs with sizes ranging from 9 to 12 nm (Fig. 3a and b), which was further confirmed by the size distribution histogram (Fig. 3c). The high-resolution TEM image indicated that the spacing between adjacent lattice planes in randomly selected G-CDs was in the range of 0.188–0.440 nm, a typical characteristic of CDs with localized graphite-like structures embedded in an amorphous carbon matrix[54,55]. The DLS particle size distribution curve of the G-CDs exhibits a single peak at 11.1 nm (Fig. 3d), indicating a relatively uniform particle size distribution that is consistent with the TEM image analysis.

The crystallinity and degree of graphitization of the G-CDs were assessed using XRD. The XRD patterns of G-CDs exhibited a broad peak centered at 2θ = 20.4° (d = 0.44 nm), indicating a predominantly amorphous structure (Fig. 3e). The lattice spacing of G-CDs is higher than the graphitic interlayer spacing of 0.33 nm, which is close to the graphite (002) plane, indicating the presence of oxygen-containing groups with sp^3 carbon and hydroxyl connected carbon groups in association with the hexagonal graphite lattice[56].

The crystallinity and amorphous morphology of the carbon structure of the G-CDs were identified using Raman spectroscopy, as shown in Fig. 3f. The Raman spectrum of the G-CDs exhibited two prominent peaks. The D-band peak at 1365 cm^{-1} belongs to sp^3 hybridized carbon, whereas the G-band peak appears at 1525 cm^{-1}, associated with sp^2 hybridized carbon[57]. The ratio of the D-band peak intensity (I_D) to the G-band peak intensity (I_G) (the I_D/I_G ratio of the G-CDs) was 1.013, which indicates that the G-CDs have a semi-crystalline structure with a high defect density[58].

Optical characterization of G-CDs

The electronic structures and optical properties of the G-CDs were investigated using UV–vis absorption spectroscopy and PL excitation (EX) and emission (EM) spectroscopy. Figure 4a shows the UV–vis absorption and PL excitation spectra of the G-CDs. The absorption spectrum was broad, with two absorption bands in the visible region at approximately 285 and 390 nm. The absorption band at 285 nm could be assigned to π–π*

Sample	Atomic Percentage (%)		
	C	N	O
GL	42.9	–	57.1
EA	44.5	25.9	29.6
G-CDs	63.0	15.1	21.9

Table 1. Carbon, nitrogen, and oxygen atomic percentage of G-CDs measured by XPS and the theoretical atomic percentage of GL and EA.
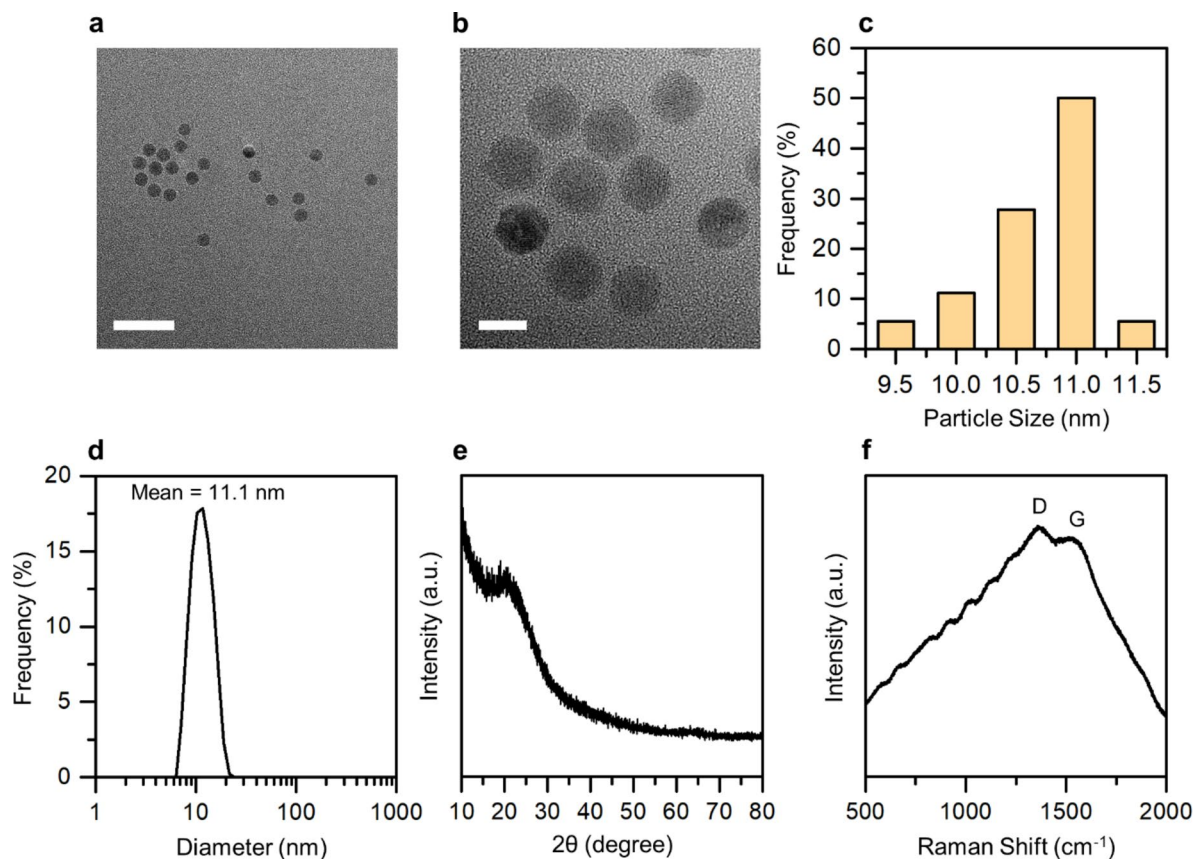
Fig. 3. (**a,b**) TEM images of G-CDs at different magnifications: (**a**) 50 and (**b**) 10 nm scale bars. (**c**) Particle size distribution of G-CDs. (**d**) DLS size-distribution curve of G-CDs. (**e**) XRD pattern of G-CDs. (**f**) Raman spectrum of G-CDs.

transitions that take place in the carbonized cores of G-CDs. The second band at 390 nm might be assigned to n-π* transition between the n-orbitals of heteroatoms (nitrogen and oxygen) and the π* orbitals of the polyaromatic domains. The PL excitation spectrum of the G-CDs at an emission wavelength of 480 nm exhibited a broad spectrum with peaks at excitation wavelengths of 250 and 400 nm, which were also attributed to π–π* transitions and n-π* transitions in the G-CDs, respectively.

The PL emission spectra of the G-CDs were examined to investigate the relationship between their PL characteristics and the presence of defect states originating from the various surface functional groups. The emission contour map (Fig. 4b) reveals a broad PL band in the visible region (450–600 nm) with the peak PL wavelength of 480 nm, attributed to the cumulative effect of the π–π* transitions of the intrinsic carbon core, as well as the n-π* transitions between various surface groups on the surface of G-CDs and the carbon core. Moreover, upon excitation from 360 to 500 nm, the G-CDs exhibited excitation wavelength-dependent emission spectra ranging from 400 to 750 nm (Fig. S5a). Such spectra are common characteristics of CDs and indicate the presence of various functional groups on the surface of the G-CDs; these groups lead to the formation of localized emissive traps that excite at different excitation energies and emit correspondingly between π and π* of C–C[59,60]. For excitation wavelengths exceeding 500 nm, the PL intensity exhibited a significant decrease of less than 5%, which aligns with the reduced light absorption in this spectral range (Fig. S5b).

The presence of deep-red to NIR absorption bands is desirable, especially for biomedical agents, because of their low degree of photon scattering, low absorption from living tissues, and deeper penetration[61,62]. Recently, several studies have reported that some CDs can emit NIR PL originating from direct recombination in the carbon core. In the carbon core, small graphitic subregions were surrounded by an oxidized amorphous core with numerous trap sites. The small graphitic subregions in the carbon core form intragap states that produce NIR PL[63]. The NIR PL emission spectrum of the G-CDs (Fig. 4c) exhibited a prominent peak at 745 nm when excited at 660 nm, indicating that the G-CDs have a well-established graphitic core state and deep-red or NIR absorption bands. The optical bandgap of the G-CDs was determined using a Tauc plot, where absorbance was plotted against photon energy following the Wood and Tauc method (Fig. 4d). The estimated direct optical bandgap energy of the G-CDs was 2.92 eV, which was closely aligned with the electronic transitions observed by PL emission spectroscopy (3.10 eV).

Pump–probe spectroscopic measurements, including those of TA and TRPL, were conducted to elucidate the PL mechanism of the G-CDs. TA spectroscopy experiments were performed in the picosecond to nanosecond time regime, pumping G-CDs with 258 nm excitation and probing them in the 370–530 nm range to investigate
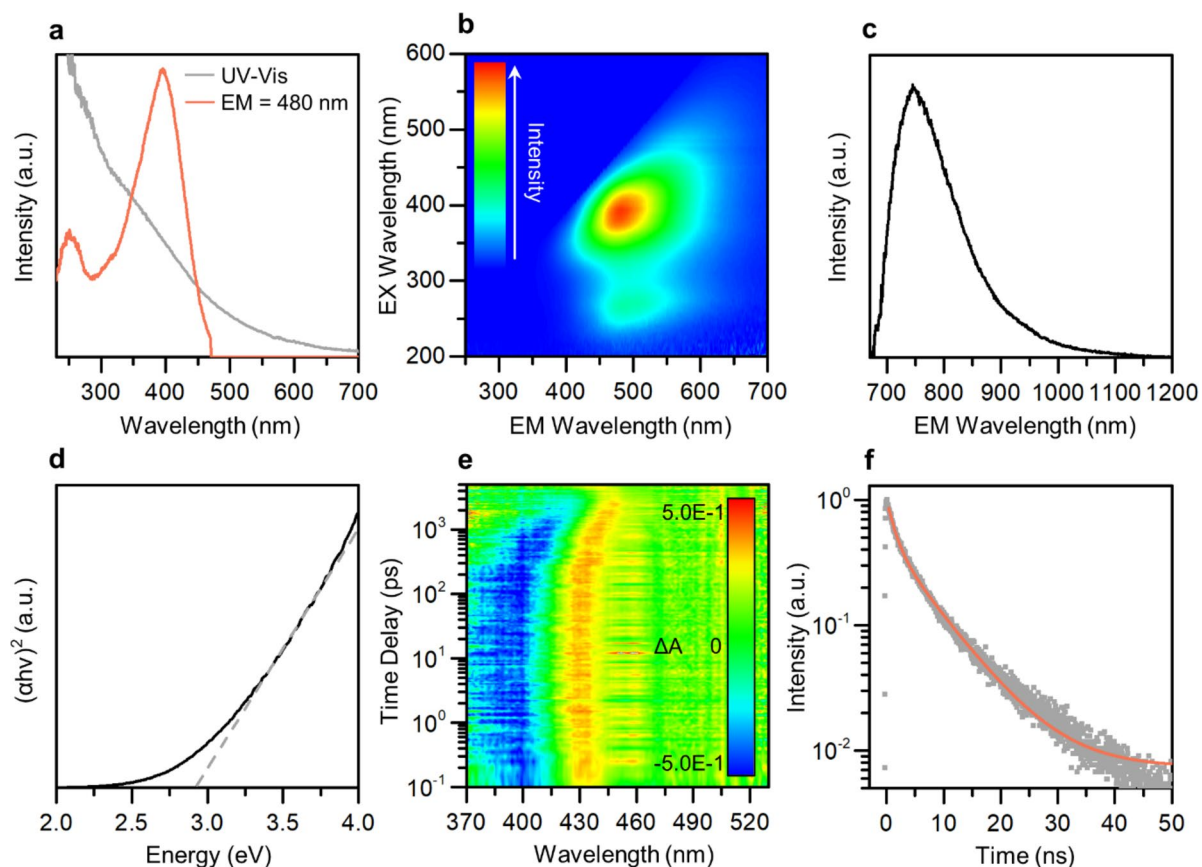
Fig. 4. (**a**) Normalized UV–vis absorption and PL excitation spectra of G-CDs. (**b**) PL emission contour map of G-CDs. (**c**) PL emission spectrum of G-CDs under 660-nm excitation light. (**d**) Tauc plot of G-CDs. (**e**) TA contour map of G-CDs excited by a 258-nm pump wavelength. (**f**) Normalized PL intensities of G-CDs at 480 nm as functions of pump exposure time under excitation at 400 nm. The solid line (red) indicates the exponential decay fitting result.

the ultrafast electron dynamics in the G-CDs (Fig. 4e). The negative (blue) features from 380 to 400 nm in the absorption signal (ΔA) correspond to ground state bleaching (GSB), a photobleaching (PB) mechanism that indicates the presence of energy states accessible to electrons photoexcited by a wavelength of 400 nm. When tracking the ΔA change over time at a probe wavelength of 400 nm, G-CDs exhibited a PB signal across all time scales (Fig. S6). The excitation spectrum at an emission wavelength of 480 nm shows a sharp peak at 400 nm, corresponding to the transition of lone-paired electrons within various intragap states. This spectral feature suggests that the PB signal is associated with the development of energetically similar energy states with different lifetimes attributed to diverse oxygen- and nitrogen-related functional groups.

The TRPL spectrum was measured at a probe wavelength of 480 nm using a pump wavelength of 400 nm to investigate the recombination dynamics of the states in G-CDs. Upon irradiation with light of an appropriate wavelength, electrons in the CDs are excited from the ground state (S_0) to the singlet first or second excited state (S_1 or S_2) via photon absorption. Electrons in S_2 quickly relax to the lowest vibrational state S_1 and then typically decay through two pathways: (1) returning to S_0 via radiative relaxation, emitting fluorescence or phosphorescence; or (2) undergoing nonradiative relaxation, generating heat or participating in photochemical reactions such as photodynamic or photocatalytic processes[64]. The TRPL spectrum of G-CDs was fitted to bi-exponential decay functions; two decay processes were identified with a radiative recombination lifetime (τ_N) of 1.44 ns and a nonradiative recombination lifetime (τ_R) of 7.15 ns (Fig. 4f). Furthermore, the absolute PL QY of the G-CDs were measured (Fig. S7). These measurements yielded QY values of 59.8 and 44.1% under 270 and 400 nm excitation, respectively. The lower QY value under 400 nm excitation indicates that the electrons located in the excited states are more likely to be dissipated via nonradiative channels than when excited at a wavelength of 270 nm. Finally, we illustrated the electronic structures of the G-CDs and the viable electronic transitions that could occur (Fig. S8).

In vitro bioimaging and photothermal characteristics of G-CDs

To assess the stability of G-CDs for potential biological applications, such as fluorescence imaging and therapy, they were exposed to air and UV light (6 W, 365 nm) for 100 h. The peak intensity was found to vary by less than ± 5%, demonstrating excellent air and UV stability (Fig. S9). Thus, the theranostic capability of G-CDs was demonstrated in vitro. In vitro cellular imaging was performed using LNCaP cells to assess the performance of

the G-CDs as bioimaging agents. After incubation of LNCaP cells in cell culture media containing G-CDs (1 mg/mL) for 24 h, the G-CDs showed bright green and deep-red fluorescence under single 488- and 633-nm laser excitation, respectively, and were observed to localize in the cytoplasmic regions through confocal microscopy (Fig. 5a). The facile cellular uptake and bright fluorescence of the G-CDs offer significant advantages for various bioimaging applications. Furthermore, G-CDs show potential for application upon excitation with NIR lasers, which exhibit deep penetration into biological tissues.

We also observed efficient cellular uptake of G-CDs, which could be mediated by the interaction of G-CDs, incorporating surface functionalities similar to those of GL with GL transporters. Among several types of GL transporters, glucose transporter type 1 (Glut1) is a transmembrane protein responsible for the passive transport of D-GL. To provide further evidence of the effect of the chemical structure of the G-CDs on cellular uptake, a flow cytometry assay based on the inhibition of Glut1 was performed. LNCaP cells were cultured for 24 h, and Glut1 was inhibited by pre-incubating the cells with STF-31. The cells were then incubated for an additional 24 h and treated with 4 mg/mL of G-CDs for 2 h. Figure 5b shows that the G-CD-treated group had a high proportion of cells with intense fluorescence, which is consistent with the confocal imaging results (control plots in Fig. S10 and the histograms in Fig. S11). Moreover, after preincubation with STF-31, the cellular uptake of G-CDs was significantly reduced by up to 25%, demonstrating the contribution of Glut1 to the cellular uptake of G-CDs (Fig. 5b and S11). The relative fluorescence intensities of G-CD-treated cells were calculated from multiple experiments, and the cells treated with STF-31 exhibited a lower fluorescence intensity than the control group without STF-31 treatment owing to the decreased cellular uptake of G-CDs (Fig. 5c), confirming that G-CDs have similar surface functionalities to GL.

Engineering nonradiative electronic states by N doping of CDs can impart photothermal conversion properties. High NIR absorption and minimal radiative transitions are crucial for efficient in vivo PTT. By reducing the energy bandgap, the light-harvesting ability is enhanced, promoting energy dissipation through nonradiative channels. This, in turn, increases the efficiency of converting absorbed light energy into heat, which is essential for achieving a high PTE. This characteristic of CDs is closely linked to their suitability for PTT applications[64–66]. When N-induced intragap states are formed, they play a major role in generating phonons (heat) via the Shockley-Read-Hall electron-hole recombination or other defect-related paths[67]. In particular, pyrrolic N-rich CDs exhibit excellent photothermal effects[68,69]. Considering that G-CDs have nitrogen-induced intragap states and exhibit two decay processes when excited at a wavelength of 400 nm, it is feasible that G-CDs exhibit photothermal performance. To examine the photothermal properties of the G-CDs, the temperature
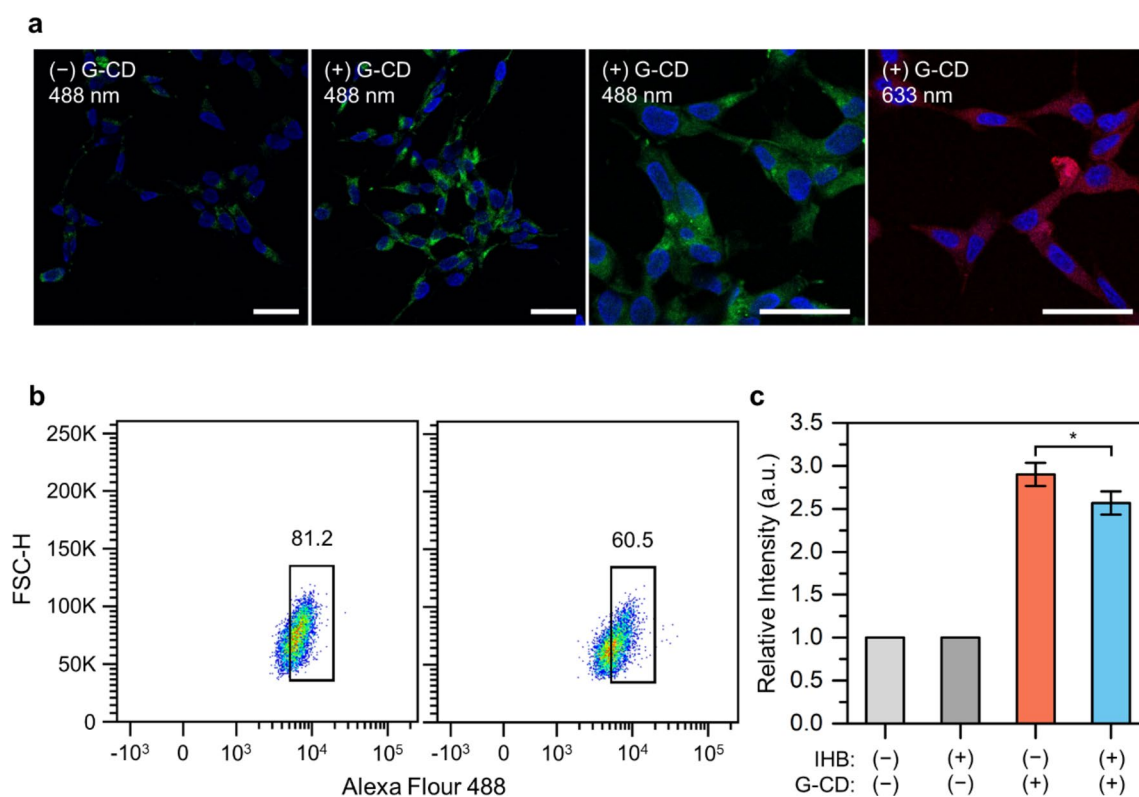

Fig. 5. (**a**) Confocal microscopy images of LNCaP cells treated with 1 mg/mL G-CDs for 24 h at different magnifications under 488- and 633-nm lasers. The cell nuclei were stained with DAPI. (Scale bar, 50 μm). (**b**) Representative flow cytometry dot plots of forward scatter versus fluorescence intensity in the Alexa Flour 488 channel for the LNCaP cells treated with G-CDs for 2 h without (left) and with (right) 24-hour STF-31 treatment. (**c**) Relative fluorescent intensity obtained using flow cytometry. Each bar represents mean ± standard deviation ($n = 4$, *$p < 0.05$ based on the unpaired Student's t-test).

changes in an aqueous solution of G-CDs at various concentrations (1–10 mg/mL) were measured under irradiation using an 808 nm NIR laser (1 W/cm^2). Because the G-CDs exhibited high absorbance at an excitation wavelength of 400 nm, an 808-nm laser was used, expecting a two-photon absorption effect. Deionized water was used as a control, and the temperature of the aqueous G-CD solutions at 1, 2, 4, and 10 mg/mL quickly increased by 7, 13.6, 20.7, and 26.4 °C from room temperature after being irradiated for 10 min, respectively (Fig. 6a). In contrast, the temperature of pure water increased by 4.2 °C under the same conditions. The excellent photothermal performance of G-CDs indicates that they are efficient photothermal agents for PTT applications.

To assess the feasibility of G-CDs for PTT of cancer, their in vitro PTT efficacy through heat generation by G-CDs was investigated in LNCaP cells under 808-nm excitation. The inherent cytotoxicity and PTT efficacy of the G-CDs were examined by measuring the relative viability of LNCaP cells treated with various concentrations of G-CDs using a cell counting kit-8 (CCK-8) assay. The viability of cells in the control group treated with blank media was set to 100%, and the relative viabilities of cells treated with 1, 2, 4, and 10 mg/mL of G-CDs were compared. As shown in Fig. 6b, LNCaP cells incubated with G-CDs at concentrations ranging from 1 to 10 mg/mL for 24 h exhibited no significant cytotoxicity, indicating that G-CDs are highly biocompatible within this concentration range and are suitable for both in vitro and in vivo biomedical applications. However, the group treated with 1 mg/mL G-CDs and irradiated with an 808-nm laser demonstrated a significant PTT effect. Increasing the concentration of G-CDs enhanced the PTT effect, with cell viability decreasing to approximately 23–29% at 10 mg/mL of G-CDs.

The effect of PTT was further demonstrated by performing a live/dead assay on LNCaP cells (Fig. 6c). After 808-nm laser irradiation at 1 W/cm^2 for 7 min, most of the cells survived in media without G-CDs; however, when the cells were treated with G-CDs in media (4 mg/mL), cell viability decreased significantly under the same laser irradiation. The cells treated with G-CDs but not irradiated with a laser showed high cell viability, which demonstrates that cell death was induced by the PTT effect and not by the G-CD itself. The low survival rate of the G-CD-treated cancer cells following laser irradiation demonstrated the high PTT efficiency of G-CDs.

Conclusion

A promising reaction mechanism for the synthesis of N-doped CDs was proposed based on the Maillard reaction using GL as the carbon source and EA as the nitrogen-doping precursor. This approach successfully preserved GL-like functionalities through mild thermal reaction conditions, imparting additional properties such as biocompatibility and targeting capabilities to the resulting CDs. The GL-like surface functionalities of the G-CDs were revealed by chemical characterization, including ^{1}H NMR and FTIR spectroscopy, as well as
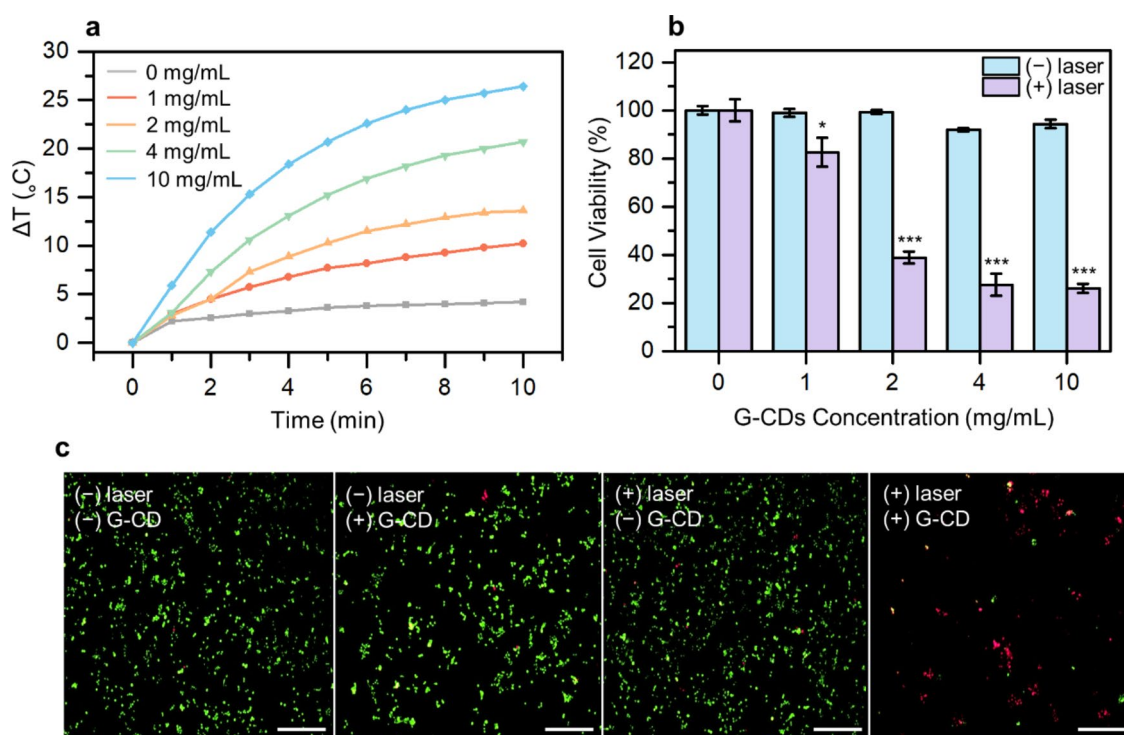

Fig. 6. (**a**) Temperature evolutions of G-CD aqueous solutions of various concentrations and pure water under 808-nm laser irradiation at 1 W/cm^2 for 10 min. (**b**) In vitro cell viability of LNCaP cells incubated with G-CDs for 24 h before and after irradiation with an 808-nm laser for 7 min. The optical density at 0 mg/mL is set to 100%. Data are represented as mean ± standard deviation ($n = 4$, *$p < 0.05$ and ***$p < 0.001$ vs. (−) laser group treated with the same G-CD concentration based on the unpaired Student's t-test). (**c**) Fluorescence images of calcein AM (green fluorescence for live cells) and polyimide (red fluorescence for dead cells) co-stained LNCaP cells treated with 4 mg mL^{-1} of G-CDs for 24 h. (Scale bar, 100 μm).

confirmed through in vitro Glut 1 inhibition experiments conducted using LNCaP cells. The electronic band structures and transitions of the G-CDs were experimentally investigated using pump–probe spectroscopy. The G-CDs exhibited NIR PL emission properties, low cytotoxicity, and heat generation ability under irradiation by an 808-nm laser, demonstrating their potential as bioimaging and PTT agents in LNCaP cells. These results indicate that the synthesized CDs inherit the functionalities of the source material, making them promising candidates for various biomedical applications.

Data availability

Data supporting the findings of this study are available in the Open Science Framework (OSF) at https://osf.io/9y2qc/?view_only=ae6b1af97de54bdab3247318a8257461.

References

1. Das, S., Mondal, S. & Ghosh, D. Carbon quantum dots in bioimaging and biomedicines. *Front. Bioeng. Biotechnol.* **11**, 1333752 (2024).
2. Pawar, S., Duadi, H., Friedman Gohas, M., Cohen, Y. & Fixler, D. Bioimaging based on poly(ethylenimine)-coated carbon dots and gold nanoparticles for pH sensing and metal enhanced fluorescence, ACS appl. *Bio Mater.* **6**, 4935–4943 (2023).
3. Zhang, W. et al. Nano-carrier for gene delivery and bioimaging based on pentaetheylenehexamine modified carbon dots. *J. Colloid Interface Sci.* **639**, 180–192 (2023).
4. Liu, C. et al. Red emissive carbon dot superoxide dismutase nanozyme for bioimaging and ameliorating acute lung injury. *Adv. Funct. Mater.* **33**, 2213856 (2023).
5. Rasheed, T. Carbon dots as robust class of sustainable and environment friendlier nano/optical sensors for pesticide recognition from wastewater. *TrAC Trends Anal. Chem.* **160**, 116957 (2023).
6. Mathew, S., Thara, C. R., John, N. & Mathew, B. Carbon dots from green sources as efficient sensor and as anticancer agent. *J. Photochem. Photobiol Chem.* **434**, 114237 (2022).
7. Panigrahi, A. et al. Exploring optoelectronic properties of undoped and amine-doped carbon dots: impact of surface functionalization and pH. *Carbon* **206**, 114–123 (2023).
8. Chaudhary, M. et al. Nitrogen-doped carbon quantum dots on graphene for field-effect transistor optoelectronic memories. *Adv. Electron. Mater.* **9**, 2300159 (2023).
9. Hao, X., Yang, Q., Liu, C. & Yang, P. Reaction-time-controlled carbon dots nanoarchitectonics with stable and bright photoluminescence for white light emission. *Dye Pigment.* **219**, 111594 (2023).
10. Fawaz, W., Hasian, J. & Alghoraibi, I. Synthesis and physicochemical characterization of carbon quantum dots produced from folic acid. *Sci. Rep.* **13**, 18641 (2023).
11. Wang, X. et al. Ultrasmall and highly biocompatible carbon dots derived from natural plant with amelioration against acute kidney injury. *J. Nanobiotechnol.* **21**, 63 (2023).
12. Zhang, S. et al. Biocompatible red blood membrane-carbon dot hybrids for near-infrared imaging-guided chemotherapy, ACS appl. *Nano Mater.* **6**, 9032–9040 (2023).
13. Zhang, T., Wang, X., Huang, H., Liu, Y. & Kang, Z. Conventional and inverted light-emitting diodes with 386 nm emission wavelength based on metal-free carbon dots. *ACS Appl. Mater. Interfaces* **15**, 18045–18054 (2023).
14. Hu, G. et al. Rational synthesis of silane-functionalized carbon dots with high-efficiency full-color solid-state fluorescence for light emitting diodes. *Carbon* **203**, 1–10 (2022).
15. Tiwari, A. et al. High quantum yield carbon dots and nitrogen-doped carbon dots as fluorescent probes for spectroscopic dopamine detection in human serum. *J. Mater. Chem. B.* **11**, 1029–1043 (2022).
16. Kumar, V. B., Mirsky, S. K., Shaked, N. T. & Gazit, E. High quantum yield amino acid carbon quantum dots with unparalleled refractive index. *ACS Nano.* **18**, 2421–2433 (2024).
17. Wu, M., Li, J., Wu, Y., Gong, X. & Wu, M. Design of a synthetic strategy to achieve enhanced fluorescent carbon dots with sulfur and nitrogen codoping and its multifunctional applications. *Small* **19**, 2302764 (2023).
18. Long, X., Wang, C., Ma, Y., Wu, S. & Hao, L. Synthesis of multiple-color emitting carbon dots by co-doping of sulfur and nitrogen. *Dye Pigment.* **209**, 110886 (2022).
19. Liu, X. et al. N-Doped carbon dots: green and efficient synthesis on a large-scale and their application in fluorescent pH sensing. *New. J. Chem.* **41**, 10607–10612 (2017).
20. Kabe, C. G. et al. The impact of the nitrogen atom on the optoelectronic, nonlinear optical, and thermodynamic properties of graphene quantum dots derived from dibenzocoronene: a DFT investigation. *Mater. Sci. Semicond. Process.* **180**, 108583 (2024).
21. Nguyen, K. G. et al. Engineering nitrogen-doped carbon quantum dots: tailoring optical and chemical properties through selection of nitrogen precursors. *Small* **20**, 2310587 (2024).
22. Wang, J. et al. High fluorescent nitrogen – doped carbon dots derived from Sanghuangporus lonicericola for detecting tetracyclines in aquaculture water and rat serum samples. *Microchem. J.* **189**, 108517 (2023).
23. Hou, J., Gao, X., Bao, S., Liu, S. & Yang, G. Yellow emissive nitrogen-doped carbon dots as a fluorescence probe for the sensitive and selective detection of silver ions. *RSC Adv.* **13**, 10508–10512 (2023).
24. Munusamy, S. et al. Nitrogen-doped carbon dots: recent developments in its fluorescent sensor applications. *Environ. Res.* **231**, 116046 (2023).
25. Nguyen, K. G. et al. Investigating the effect of N-doping on carbon quantum dots structure, optical properties and metal ion screening. *Sci. Rep.* **12**, 13806 (2022).
26. Rodríguez-Carballo, G. et al. Nitrogen doped carbon dots as a photocatalyst based on biomass. A life cycle assessment. *J. Clean. Prod.* **423**, 138728 (2023).
27. Balou, S., Shandilya, P. & Priye, A. Carbon dots for photothermal applications. *Front. Chem.* **10**, 1023602 (2022).
28. Liu, Y. et al. Nitrogen doped carbon dots: mechanism investigation and their application for label free CA125 analysis. *J. Mater. Chem. B* **7**, 3053–3058 (2019).
29. Zhang, L., Wei, S., Zhang, L., Yin, X. & Yang, R. A novel type of fluorescence modulation mechanism of carbon dots derived from the competition of photoinduced electron transfer and fluorescence. *Spectrochim Acta Mol. Biomol. Spectrosc.* **304**, 123276 (2024).
30. Gómez, I. J. et al. Spontaneous formulation of carbon dots helps to distinguish molecular fluorophores species. *Appl. Surf. Sci.* **610**, 155536 (2023).
31. Ran, Z., Liu, J., Zhuang, J., Liu, Y. & Hu, C. Multicolor afterglow from carbon dots: preparation and mechanism. *Small Methods* **8**, 2301013 (2024).
32. Ganguly, S. et al. Microwave-synthesized polysaccharide-derived carbon dots as therapeutic cargoes and toughening agents for elastomeric gels. *ACS Appl. Mater. Interfaces* **12**, 51940–51951 (2020).

33. Dubey, N., Dhiman, S. & Koner, A. L. Review of carbon dot-based drug conjugates for cancer therapy, ACS appl. *Nano Mater.* **6**, 4078–4096 (2023).

34. Azizi, M. et al. Synthesis of self-targeted carbon dot with ultrahigh quantum yield for detection and therapy of cancer. *ACS Omega* **5**, 24628–24638 (2020).

35. Ghosh, T., Das, T. K., Das, P. & Banerji, P. Ch. Das, current scenario and recent advancement of doped carbon dots: a short review scientocracy update (2013–2022). *Carbon Lett.* **32**, 953–977 (2022).

36. Dubey, N., Ramteke, S., Jain, N. K., Dutta, T. & Koner, A. L. Glucose-derived carbon dots for targeted delivery of doxorubicin in cancer therapy. *New. J. Chem.* **47**, 16390–16398 (2023).

37. Das, P. et al. Naturally derived carbon dots in situ confined self-healing and breathable hydrogel monolith for anomalous diffusion-driven phytomedicine release. *ACS Appl. Bio Mater.* **5**, 5617–5633 (2022).

38. Boakye-Yiadom, K. O. et al. Carbon dots: applications in bioimaging and theranostics. *Int. J. Pharm.* **564**, 308–317 (2019).

39. Yuan, X., Zhang, X., Sun, L., Wei, Y. & Wei, X. Cellular toxicity and immunological effects of carbon-based nanomaterials. *Part. Fibre Toxicol.* **16**, 18 (2019).

40. Lalwani, G., D´agati, M., Khan, A. M. & Sitharaman, B. Toxicology of graphene-based nanomaterials. *Adv. Drug Deliv. Rev.* **105**, 109–144 (2016).

41. Van Boekel, M. A. J. S. Formation of flavour compounds in the Maillard reaction. *Biotechnol. Adv.* **24**, 230–233 (2006).

42. Tamanna, N. & Mahmood, N. Food Processing and Maillard reaction products: Effect on Human Health and Nutrition. *Int. J. Food Sci.* **2015**, 526765 (2015).

43. Thorpe, S. R. & Baynes, J. W. Maillard reaction products in tissue proteins: new products and new perspectives. *Amino Acids* **25**, 275–281 (2003).

44. Mishra, R. K., Pulidindi, I. N., Kabha, E. & Gedanken, A. In situ formation of carbon dots aids ampicillin sensing. *Anal. Methods.* **8**, 2441–2447 (2016).

45. De, B. & Karak, N. A green and facile approach for the synthesis of water soluble fluorescent carbon dots from banana juice. *RSC Adv.* **3**, 8286–8290 (2013).

46. Kurdekar, A. et al. Comparative performance evaluation of carbon dot-based paper immunoassay on Whatman filter paper and nitrocellulose paper in the detection of HIV infection. *Microfluid Nanofluidics* **20** 99 (2016).

47. Nair, S. S. P., Kottam, N. & Kumar, S. P. Green synthesized luminescent carbon nanodots for the sensing application of Fe^{3+} ions. *J. Fluoresc.* **30**, 357–363 (2020).

48. Trpkov, D. et al. Hybrid nanostructures of nitrogen-doped carbon dots and aromatic amino acids: synthesis, interactions at interfaces and optical properties. *Colloids Surf. B Biointerfaces.* **238**, 113878 (2024).

49. Kumar, B. P., Salikolimi, K. & Eswaramoorthy, M. Glucose-and pH-responsive charge-reversal surfaces. *Langmuir* **30**, 4540–4544 (2014).

50. Sharma, A. & Das, J. Small molecules derived carbon dots: synthesis and applications in sensing, catalysis, imaging, and biomedicine. *J. Nanobiotechnol.* **17**, 92 (2019).

51. Wang, S. et al. Single-atom manganese anchored on carbon dots for promoting mitochondrial targeting and photodynamic effect in cancer treatment, ACS appl. *Nano Mater.* **5**, 6679–6690 (2022).

52. Wu, X. et al. Enhanced chemodynamic and photoluminescence efficiencies of Fe–O4 coordinated carbon dots via the core–shell synergistic effect. *Nanoscale* **15**, 376–386 (2023).

53. Le, P. et al. Multifunctional applications for waste zinc–carbon battery to synthesize carbon dots and symmetrical solid-state supercapacitors. *RSC Adv.* **12**, 10608 (2022).

54. Sun, X., Bruckner, C. & Lei, Y. One-pot and ultrafast synthesis of nitrogen and phosphorus co-doped carbon dots possessing bright dual wavelength fluorescence emission. *Nanoscale* **7**, 17278–17282 (2015).

55. Chunduri, L. A. A. et al. Carbon quantum dots from coconut husk: evaluation for antioxidant and cytotoxic activity. *Mater. Focus.* **5**, 55–61 (2016).

56. El-Shafey, A. M. Carbon dots: Discovery, structure, fluorescent properties, and applications. *Green. Process. Synth.* **10**, 134–156 (2021).

57. Liu, H., Zhang, Y. & Huang, C. Development of nitrogen and sulfur-doped carbon dots for cellular imaging. *J. Pharm. Anal.* **9**, 127–132 (2019).

58. Li, Z., Deng, L., Kinloch, I. A. & Young, R. J. Raman spectroscopy of carbon materials and their composites: Graphene, nanotubes and fibres. *Prog Mater. Sci.* **135**, 101089 (2023).

59. Goryacheva, I. Y., Sapelkin, A. V. & Sukhorukov, G. B. Carbon nanodots: mechanisms of photoluminescence and principles of application. *TrAC Trends Anal. Chem.* **90**, 27–37 (2017).

60. Wang, X. et al. Voltage-dependent photoluminescence of carbon dots. *J. Electrochem. Soc.* **167**, 147515 (2020).

61. Liu, Y. et al. Research progress on near-infrared long persistent phosphor materials in biomedical applications. *Nanoscale Adv.* **4**, 4972–4996 (2022).

62. Hussain, M. M., Khan, W. U., Ahmed, F., Wei, Y. & Xiong, H. Recent developments of Red/NIR carbon dots in biosensing, bioimaging, and tumor theranostics. *J. Chem. Eng.* **465**, 143010 (2023).

63. Park, Y. et al. Unraveling the origin of near-infrared emission in carbon dots by ultrafast spectroscopy. *Carbon* **188**, 229–237 (2021).

64. Zhang, T., Wu, J., Tang, Z. & Qu, S. Tuning the photothermal properties of carbon dots in the deep-red to near-infrared wavelength regions for tumor therapy. *Mater. Chem. Front.* **7**, 2359–2372 (2023).

65. Liu, J., Li, R. & Yang, B. Carbon dots: a new type of carbon-based nanomaterial with wide applications. *ACS Cent. Sci.* **6**, 2179–2195 (2020).

66. Wu, Y. et al. Fabrication of manganese-coordinated polyphenol carbon dots for photothermal therapy and immune activation. *Cancer Nano* **13**, 30 (2022).

67. Park, Y. et al. Biocompatible nitrogen-doped carbon dots: synthesis, characterization, and application. *J. Mater. Chem. B.* **8**, 8935–8951 (2020).

68. Permatasari, F. A., Fukazawa, H., Ogi, T., Iskandar, F. & Okuyama, K. Design of pyrrolic-N-rich carbon dots with absorption in the first near-infrared window for photothermal therapy, ACS appl. *Nano Mater.* **1**, 2368–2375 (2018).

69. Yang, K. et al. In vitro and in vivo near-infrared photothermal therapy of cancer using polypyrrole organic nanoparticles. *Adv. Mater.* **24**, 5586–5592 (2012).

Acknowledgements

Author contributions

Soohyun Cho: Methodology, Investigation, Writing – Original Draft, Visualization. Hyemin Kim: Methodology, Investigation, Writing – Original Draft, Visualization. Dongwook Song: Investigation, Validation. Jungchan Jung: Investigation, Validation. Sehyeon Park: Investigation, Validation. Hyunda Jo: Validation. Sejeong Seo: Validation. Chaewon Han: Validation. Soye Park: Validation. Hyunho Han: Conceptualization, Methodology, Writing, Review & Editing. Woosung Kwon: Conceptualization, Methodology, Writing – Review & Editing, Supervision.

Declarations

Competing interests

The authors declare no competing interests.

Additional information

Supplementary Information The online version contains supplementary material available at https://doi.org/10.1038/s41598-024-82767-z.

Correspondence and requests for materials should be addressed to W.K. or H.H.

Reprints and permissions information is available at www.nature.com/reprints.

Publisher's note Springer Nature remains neutral with regard to jurisdictional claims in published maps and institutional affiliations.